Shear transformation distribution and activation in glasses at the atomic scale

F. Boioli, T. Albaret, and D. Rodney
Institut Lumière Matière, UMR5306 Université Lyon 1-CNRS, Université de Lyon, F-69622 Villeurbanne Cedex, France
(Received 26 December 2016; published 28 March 2017)

We characterize shear transformations (STs) at the atomic scale in a model of amorphous silicon using a mapping on Eshelby inclusions. We investigate the effect of pressure, glass relaxation, as well as damage on the ST characteristics. We show that the characteristic ST effective volume, $\gamma_0 V_0$, product of the ST plastic shear strain γ_0 and volume V_0, does not depend significantly on an applied pressure but increases with accumulated plastic deformation from about 10 Å^3 in the pseudoelastic regime to about 60 Å^3 once plastic flow sets in. Furthermore, by using nudged elastic band calculations, we measure the energy barrier against ST activation. Analyzing different paths leading to either an isolated ST or an avalanche, we show that the barrier is systematically controlled by the first ST with an activation volume equal to the effective volume of the ST at the activated state, which represents only a fraction of the complete ST volume. The activation volume is also found smaller for avalanches, presumably because of accumulated local damage. This work provides essential information to build reliable mesoscale models of plasticity.

DOI: 10.1103/PhysRevE.95.033005

I. INTRODUCTION

Amorphous solids are characterized by a high strength but a low ductility [1–3], due to a pronounced localization of the plastic deformation in shear bands, leading to catastrophic failure [4] and preventing the use of glasses as structural materials [2]. Understanding plastic deformation in glasses and its localization in shear bands is therefore of utmost importance.

It is generally accepted that the elementary process underlying plastic deformation in amorphous solids involves the local rearrangement of small numbers of atoms [5–8]. These events are commonly referred to as shear transformations (STs) [6] or shear transformation zones (STZs) [8,9]. Although details of the ST structure, size, and energetics may vary from glass to glass, STs have been observed in many simulation studies, covering different amorphous materials, from metallic glasses [8,10,11] to amorphous silicon [12,13]. Also direct evidence of STs was found in deformation experiments on bubble rafts [5] and colloidal glasses [14].

STs are at the core of mesoscale models of plasticity [9,15–20], which, despite differences in their detailed implementation, all assume that macroscopic plasticity results from the accumulation of STs that interact elastically and can organize at the micron scale to form shear bands. Based on Eshelby's theory [21], STs are modeled as homogeneous plastic inclusions in a continuous elastic matrix and are defined by their volume V_0 and plastic strain γ_0, which have been estimated in the case of metallic glasses from experimental data [17]. Another important feature is that STs are thermally activated, which has been modeled at the mesoscale by using a kinetic Monte Carlo algorithm [9,15,17]. This approach relies on an activation rate proportional to the Boltzmann probability that the system overcomes the activation barrier associated with the nucleation of a ST:

$$\dot{s} = \nu_0 \exp\left(-\frac{\Delta H}{k_B T}\right), \tag{1}$$

where ν_0 is the attempt frequency to jump over the enthalpy barrier ΔH and $k_B T$ is the thermal energy. As proposed in Ref. [15], the barrier to activate a ST under an applied shear stress τ is written as

$$\Delta H = \Delta E - \tau V_0 \gamma_0^*, \tag{2}$$

where ΔE is the activation energy in absence of applied stress. The second term in Eq. (2) is the work done by the applied stress between the initial and activated states of the ST, assuming that the activated state has the same volume V_0 as the full ST and a plastic shear strain γ_0^*. The product $\Delta V^* = V_0 \gamma_0^*$ is the ST activation volume, which reflects the sensitivity of the activation barrier on the applied shear stress.

Usually, the parameters ν_0, V_0, γ_0, ΔE of the elastoplastic models are kept constant for all STs [9,17] or are drawn from phenomenological statistical distributions [18,22,23] that have not been verified at the microscopic scale. However, a local dependence of ΔE on an internal state variable related to the local excess free volume can be introduced to take into account local damage which leads to an improved description of the shear band formation [24]. These local fluctuations are in broad agreement with the widely distributed activation energies and attempt frequencies found from atomistic explorations of the the potential energy landscape of glasses [25–27]. More recently, Albaret *et al.* [12] measured effective volumes of STs in atomistic models of amorphous silicon and also found distributions, albeit exponential, justifying the use of characteristic values for V_0 and γ_0. Still, the general consistency between the mesocopic model and the atomistic scale simulation has been obtained from simplifying assumptions and simple loading conditions. Potentially important effects related to the level of glass relaxation and damage [28] have not been considered to extract effective volumes in Ref. [12] while the loading was restricted to simple shear. Nonetheless, pressure and normal stresses are known to strongly affect plastic flow in disordered solids. This is the case of metallic glasses, where neither the von Mises nor Tresca yield criteria, which depend only on the deviatoric part of the stress tensor, are well adapted, while the Mohr-Coulomb criterion, which takes into account the effect of normal stress components, gives more satisfactory results [29,30]. Also, the activation volumes of the STs used

in Eq. (2) should be evaluated at the transition state. Homer *et al.* [17] assumed that this activated state is at the middle of the transition path with a plastic strain $\gamma_0^* = \gamma_0/2$ and an activation volume $\Delta V^* = \gamma_0 V_0/2$, where $\gamma_0 V_0$ corresponds to the fully relaxed effective volume after the transformation. Up to now, the effective volumes extracted from atomistic simulations are also associated with fully relaxed state. It is therefore interesting to evaluate the STs transformation paths through atomistic simulations, to access both the activation volumes and the transient dilatation effects, which are often incorporated in ST mesoscopic models [6,24,31].

Here, we extend the characterization of STs from the atomic scale initiated by Albaret *et al.* [12] to investigate the effect of pressure, glass relaxation, as well as of damage on the ST characteristics. We focus on the STs effective volumes which represent explicit parameter in mesoscopic models. Additionally, we explore the thermal activation of STs by measuring directly their enthalpy barriers using the nudged elastic band (NEB) method [32]. In doing so, we test in Eq. (2) the relation between the activation volume ΔV^* and the effective ST volume $V_0\gamma_0^*$ at the activated state. To this end, we consider both simple and complex events, corresponding to the activation of either an isolated ST or an avalanche of STs.

II. METHODOLOGY

Amorphous silicon (a-Si) is a prototypical amorphous solid, which provides generic insights into the mechanical behavior of glasses. Models of a-Si were obtained by following a procedure similar to Ref. [13]. The samples consist of 32 768 atoms interacting through the Stillinger-Weber (SW) potential [33]. A three-dimensional simulation box with a linear size of about 87 Å was used. The amorphous configurations were obtained by quenching at 10^{11} K/s a liquid equilibrated at 3500 K down to 0 K. The atomic positions were further relaxed until the maximum force on all atoms was below 10^{-3} eV/Å. The cell size was also relaxed until the pressure was below 0.5 MPa. The effect of pressure and normal stresses on the plastic properties of a-Si was investigated through athermal quasistatic deformations. Constant normal stress components were imposed by adapting the cell size using an Andersen barostat [34]. A shear strain increment $\delta\gamma = 1\times10^{-3}$ in the xy plane was employed. After each strain increment, the potential energy was minimized using the same force criterion as above.

A similar protocol was employed to access the activation properties of STs. In this case, simple shear deformation simulations were performed at constant volume. In order to identify mechanically stable states between elementary or complex plastic events, a smaller strain increment $\delta\gamma = 2\times10^{-5}$ was used and the amorphous configuration was relaxed until the maximum force was less than 1×10^{-5} eV/Å. Starting from minimum energy configurations, standard NEB calculations [32,35,36] were performed to identify transition paths associated with plastic events.

STs were identified and characterized following the methodology presented in Ref. [12]. Details on the method can be found therein. Briefly, this procedure can be summarized in three steps. First, STs are identified from the variation of the local potential energy, which provides a measure of the local plastic activity. The plastic activity around each local maximum can be well approximated by a decaying exponential function, whose characteristic length λ is taken as the ST size. The ST is then assumed spherical with a volume $V_0 = \frac{4}{3}\pi\lambda^3$. Finally, the ST plastic strain is extracted by taking advantage of the Eshelby inclusion theory [21]. Namely, the atomic displacements in the simulation cell are fitted on a collection of Eshelby inclusions, to extract for each inclusion the full Eshelby strain tensor $\bar{\bar{\varepsilon}}_0$. The plastic shear strain γ_0 is then calculated as the largest difference between the eigenvalues of the deviatoric part of the strain tensor.

III. IMPACT OF PRESSURE ON THE SHEAR DEFORMATION IN A-SI

Shear simulations under a constant pressure P varying from $+10$ GPa in compression and -10 GPa in tension are shown in Fig. 1. The resulting yield stresses σ_Y, taken as the maximum stress along the stress-strain curves, is plotted in Fig. 1(b) as a function of P. Both σ_Y and P are normalized by the yield stress σ_{Y0} obtained at $P = 0$. Before the yield point, the shear stress shows the same trend at all pressures. A quasilinear stress-strain relationship is found at small deformation, indicating a dominant elastic behavior. Irreversible plastic deformation increases in intensity at larger γ values, beyond which plastic flow sets in except at $P = -10$ GPa (this case will be discussed below).

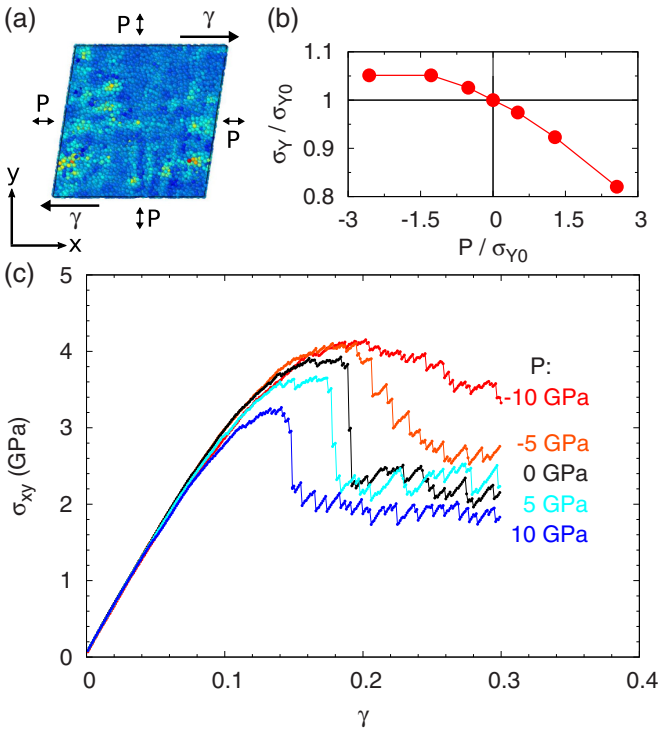

FIG. 1. Quasistatic shear deformation simulations under a constant pressure P. (a) Sketch of the loading conditions: positive shear strain increments $\delta\gamma_{xy}$ are applied in the xy plane, giving rise to a total strain γ and shear stress σ_{xy}, at a constant pressure P. (b) Yield stress σ_Y as a function of the applied pressure P. Both σ_Y and P are normalized by $\sigma_{Y,0}$, the yield stress at $P = 0$ GPa. (c) Stress-strain curves obtained under quasistatic shear at a constant applied pressure P, ranging from -10 to 10 GPa.

The behavior in tension and compression is asymmetrical. As shown in Fig. 1(b), the yield stress remains approximately constant in tension while it decreases in compression. Furthermore, the onset of plastic flow occurs at smaller γ values in compression compared to tension. These asymmetries indicate a more ductile behavior of the a-Si sample in compression, suggesting that ST activation is facilitated in this case. This finding is explained by the peculiarity of the present SW potential that favors five- rather than threefold coordinated defects [13,37,38]. Accordingly, atomistic rearrangements producing over-coordinated atoms around the ST cores are more easily obtained and induce local densifications. This analysis is supported by the negative trace of the average Eshelby strain tensors $\bar{\bar{\varepsilon}}_0$ distribution that was already evidenced in a previous work [12] and that we will confirm below. The activation of STs is therefore helped under compression, leading to the more ductile behavior seen in Fig. 1. This behavior is rather unusual among glasses, where plastic events classically create excess free volume and therefore induce local dilatations [39,40]. Note that this result relies on the actual bond character and directionality of the present SW interaction potential [12,13], these parameters therefore play a critical role in the activation of STs, reversing the usual sign of dilatation by plastic deformation. This will also be evident from the characterization of ST activation paths in Sec. IV.

Normal stresses also influence the way STs organize. We see in Fig. 1(c) that the first shear band, which is marked by a large stress drop, occurs at increasing γ when we move from compression ($P > 0$) to tension ($P < 0$). The case $P = -10$ GPa is particular because no shear band occurs until $\gamma \sim 0.3$, the point at which the glass fails and fractures in two halves. Compressive stresses therefore facilitate the activation of STs and lead to early shear bands, the latter are stabilized by the confining pressure allowing for steady-state shear flow. In tension the system displays less plastic activity with a more homogeneous distribution of STs and a slightly higher yield stress. At the negative pressure $P = -10$ GPa, the sample attempts to form a shear band at $\gamma \sim 0.3$ but the resulting local damage weakens too much the glass, which can no longer sustain the tensile stresses and breaks.

A. Stress-strain curves from Eshelby model

Plastic events in simple shear atomistic simulations of a-Si were successfully mapped onto a collection of Eshelby inclusions in Ref. [12]. This allows one to reproduce with accuracy the atomistic stress-strain curve and justifies the usual decomposition of plasticity into STs. In the following, we show that the Eshelby model also applies well when normal-stress components are considered.

The shear stress variation induced by each Eshelby inclusion depends on the elastic shear modulus G, Poisson's ratio ν, and on the characteristic volume V_0 and xy plastic strain tensor component $\varepsilon_{xy,0}$ of the inclusion. By taking into account the contribution of all the STs identified during the quasistatic shear deformation simulations, we calculated the resulting shear stress as a function of γ. In Fig. 2, we compare the atomistic stress strain curves (solid lines) with the shear stress predicted by the Eshelby inclusion model (dashed gray lines). The curves obtained by imposing P from -10 to 10 GPa are shown. Similar results were obtained by applying a normal stress along either the x or y directions. As seen in Fig. 2, the Eshelby model reproduces well the atomistic stress-strain curves. The discrepancy between the atomistic results and the model predictions, noticeable on the curves, originates from the accumulation of small errors in fit of the Eshelby strain for each event. This is mainly due to the difficulties to clearly separate plastic events and to the local fluctuations due to the discrete atomic structure. On one side the displacements associated with weak plastic events originate mainly from the local fluctuations due to the discrete atomic structure, which cannot be represented by the continuum expressions. On the other, when large stress drops associated with shear bands occurs, too much overlap between STs prevents to clearly separate them (these events can collect up to few hundred inclusions), resulting in a less accurate fit of the Eshelby strain.

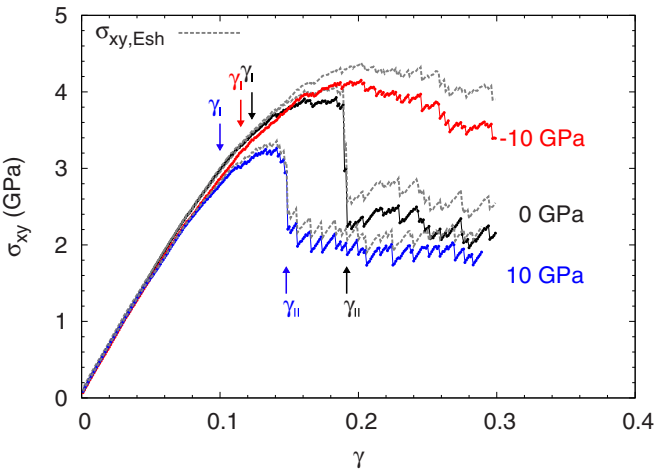

FIG. 2. Comparison between stress-strain curves obtained with atomistic simulations (solid color lines) and Eshelby model (dashed gray lines) for different values of the applied pressure.

B. Distributions of ST effective volume and trace

1. Pressure and effective volumes

In order to establish a link between atomic-scale properties and ST representation in mesoscale models, we analyzed the STs identified in the atomistic simulations using the Eshelby formalism. In Fig. 3, we report the distribution of effective volumes $\gamma_0 V_0$, i.e., the product of the Eshelby shear strain and volume. This effective volume appears in the classical expression of the ST activation volume [Eq. (2)] and while in our analysis, V_0 can be defined in different ways, resulting in different γ_0 distributions, the distribution of $\gamma_0 V_0$ is uniquely defined [12].

In order to investigate the potential dependence of the effective volume on damage and therefore, on the applied deformation, we determined the distribution of $\gamma_0 V_0$ in three different regimes: (I) the quasielastic regime for $0 < \gamma < \gamma_{\rm I}$, where $\gamma_{\rm I}$ is determined by a stress deviation of 20% respect to an ideal elastic stress $\sigma^{\rm el} = \gamma G_{\gamma=0}$; (II) the regime of plastic transition spans from $\gamma_{\rm I}$ to $\gamma_{\rm II}$, where $\gamma_{\rm II}$ corresponds to the first shear band (including it); and (III) the regime of plastic flow after the first shear band ($\gamma > \gamma_{\rm II}$). Although these three

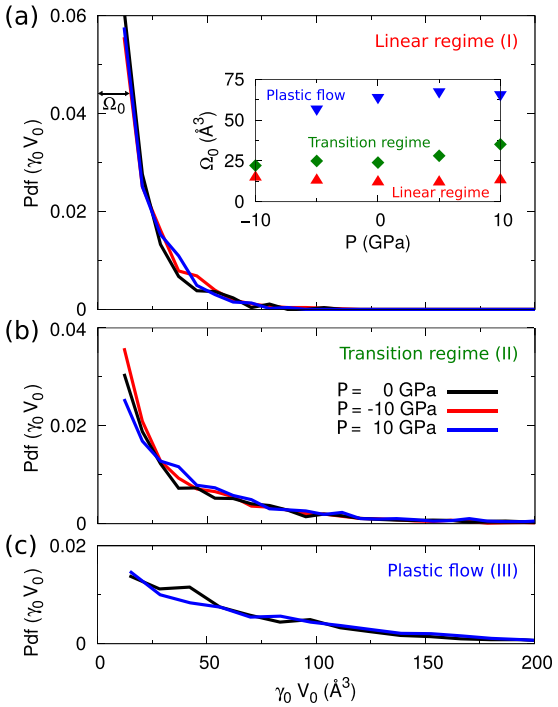

FIG. 3. Probability density function (Pdf) of the effective Eshelby volume $\gamma_0 V_0$ in different regions of strain: (a) $\gamma < \gamma_I$ ($\sim$0.1), the deformation is mainly elastic; (b) $\gamma_I \leqslant \gamma \leqslant \gamma_{II}$, transition region, which contains the yield stress and the first shear band; (c) $\gamma > \gamma_{II}$, plastic flow. γ_{II} varies with the applied pressure P and corresponds to the development of the first shear band. Three pressures, from -10 to $+10$ GPa are considered. Inset: characteristic effective volume Ω_0, calculated as the width of the $\gamma_0 V_0$ distributions fitted with a decaying exponential function, as a function of P in the three selected γ ranges.

regimes are determined with the same rules, they lead to strain ranges that depend on the normal stress state with the particular case of $P = -10$ GPa, which has no third regime. Actual values of γ_I and γ_{II} are shown in Fig. 2.

As shown in Fig. 3, the distributions are rapidly decreasing and they can be well fitted by decaying exponentials, allowing us to define characteristic effective volumes, noted here Ω_0. The latter is reported in the inset of Fig. 3(a) in the three strain regions as a function of the applied pressure. In the first regime, which is quasielastic, the distributions of effective volumes are not affected by the applied pressure. The characteristic size of the distribution is approximately constant, with $\Omega_0 = 13 \pm 1$ Å^3. In the second regime, where plastic flow begins, the $\gamma_0 V_0$ distributions under a negative pressure do not differ from the one obtained at $P = 0$ GPa. The characteristic effective volume Ω_0 increases with respect to the first regime, with $\Omega_0 = 25 \pm 2$ Å^3 for P ranging from -10 to 5 GPa. A broader distribution with $\Omega_0 = 35 \pm 1$ Å^3 is found at $P = 10$ GPa, probably linked to the damage induced by the enhanced plastic activity in compression. More widespread distributions are obtained in the third regime of plastic flow: Ω_0 varies from 57 ± 1.5 Å^3 to 64 ± 1.5 Å^3 when P increases from -5 GPa to 0 GPa and remains approximately constant in compression.

The main outcome from Fig. 3 is that the characteristic Eshelby volume Ω_0 increases with deformation: with the exception of $P = 10$ GPa, the characteristic volume is low, between $\sim$ 13 and 25 Å^3 until the plastic flow sets in and then increases up to about 65–70 Å^3 in the plastic flow. STs are therefore larger in size when they occur in a glass damaged by shear bands compared to the initial well-relaxed glass. On the other hand, the distributions of $\gamma_0 V_0$ are not strongly affected by pressure. The larger Ω_0 value obtained at $P = 10$ GPa in the intermediate regime can be attributed to the enhanced plastic activity leading to early onset of shear banding in compression. The transition between the second and third regime is quite sharp in compression and at zero pressure, but is not as well defined at $P = -5$ GPa as denoted by the smaller amplitude of the stress drop associated with the first shear band ($\gamma = 0.206$) in the stress-strain curve. This may explain the smaller Ω_0 value obtained at $P = -5$ GPa in the third regime. From this analysis, the marked differences observed in Fig. 1 between the stress-strain curves are mainly due to the pressure dependence of the strain ranges that determine the different regimes. Under a large tensile stress ($P = -10$ GPa) the lower plastic activity is associated with a system that experiences a unique regime with small effective volumes STs over the whole strain range.

The decaying exponential distributions of $\gamma_0 V_0$ obtained under the influence of pressure extend the validity of the assumption of a constant effective volume adopted in mesoscale models and show that the characteristic ST shear strain is not strongly affected by pressure or normal stresses. In mesoscale simulations of plasticity in amorphous metals, $\gamma_0 \sim 0.1$ [15] and $V_0 \sim$ 800–1600 Å^3 [9,17,24] have been used, leading to $\gamma_0 V_0 \sim$ 80–160 Å^3. This value is larger, but of the same order as that found here. However, a more complex behavior results from the present atomic-scale ST analysis, suggesting that the effective ST volume should increase with the accumulated deformation and converge to a constant value only after the development of shear bands.

2. *Effect of glass relaxation on effective volumes*

To further analyze the effect of damage on STs, we calculated the distributions of Ω_0 in the three regimes described above for three a-Si samples obtained at different quench rates (10^{11}, 2×10^{12}, and 3×10^{16} K/s). The shear deformation for these samples were done at constant volume with pressures in the range $-1 < P < 0$ GPa. In the first regime, we obtained a larger Ω_0 value (28.5 ± 0.5 Å^3) only for the less relaxed structure (i.e., highest quench rate), and in the second and third regimes we found no influence of the initial level of relaxation on the distributions, which is expected since the accumulated plastic deformation erases the memory of the initial state. The initial level of relaxation has therefore a weaker impact on the distributions of Ω_0 than the damage induced by shear-banding. A marked effect is only apparent in samples prepared at extremely high quenching rate where the first and second regimes almost collapse with a single characteristic effective volume.

3. *Local volume variation*

The asymmetric mechanical response in tension and compression of the a-Si sample is better explained by investigating the change of volume generated by STs. To characterize the

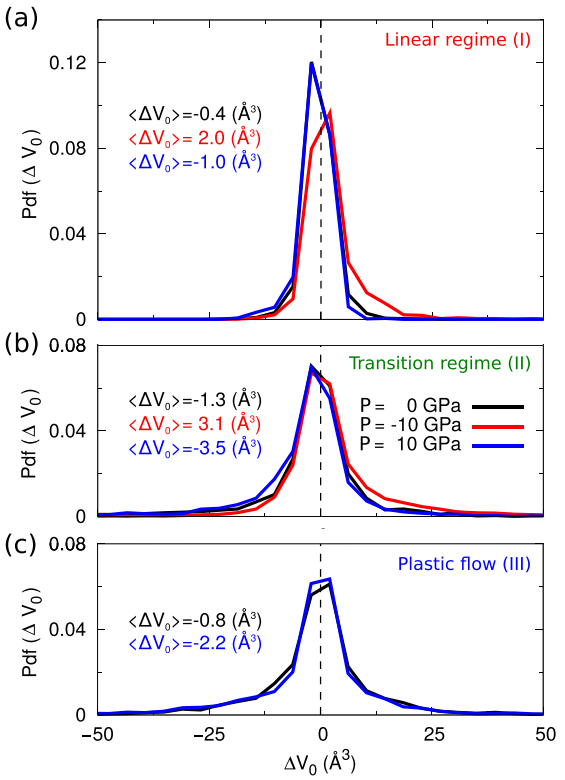

FIG. 4. Probability density function (Pdf) of the Eshelby volume variation $\Delta V_0 = \varepsilon_{\mathrm{Tr}} V_0$ in the same three strain regimes described in the caption of Fig. 3. $\varepsilon_{\mathrm{Tr}}$ is the trace of the Eshelby strain tensor and V_0, the Eshelby volume.

volume variation induced by STs, we reported in Fig. 4 the distributions of $\varepsilon_{\mathrm{Tr}} V_0$, where $\varepsilon_{\mathrm{Tr}}$ is the trace of the Eshelby strain transformation tensor $\bar{\bar{\varepsilon}}_0$ and V_0, the ST volume. As for the effective Eshelby volume $\gamma_0 V_0$, we observe a progressive broadening of the $\varepsilon_{\mathrm{Tr}} V_0$ distributions with increasing γ, from the linear to the transition regime. The distribution averages are shifted towards increasing volume for decreasing values of the pressure. In agreement with the tendency of the present SW potential to produce over-coordinated atoms and local densification, the average ST volume variation remains negative in all the regimes under compression and at zero pressure. Under tension, the average ST volume variation can however become positive, that means that the average nature of the underlying STs should differ from the typical ST which involves production of over-coordinated defects. In the third regime the amplitude of the average volume variation decreases. Such a behavior is consistent with an evolution towards a steady state where the plastic events occur in a damaged glass, which already contains a large fraction of defective Si atoms, resulting in no volume change on average.

This asymmetric distribution of characteristic ST hydrostatic strain is consistent with the more ductile behavior observed in compression. It has been shown that STs tend to localize on over-coordinated local defects that they themselves produce, leading to an enhanced plasticity interpreted as an autocatalytic effect already pointed out in previous studies [13,38,41]. Therefore, STs inducing a volume contraction are favored in this material, they are prone to organize in a strongly correlated manner to produce shear banding. Since these STs imply local densification, these effects are enhanced under compressive normal components. On the contrary, STs associated with local volume contractions cannot accommodate an imposed tension, and STs with an average dilatation are instead obtained. No autocatalytic effect is expected in this case and the overall plastic activity is reduced and homogeneously distributed. To conclude, we assign the asymmetric pressure behavior in these SW samples to the different nature of the STs implied either in compression or in tension.

IV. ST ACTIVATION BY NUDGED ELASTIC BAND CALCULATIONS

The energy barriers and activation volumes involved in plastic rearrangements are other important parameters for mesoscale models, required to address the strain-rate sensitivity of glass plasticity. To extract these quantities from atomistic simulations, the activation path of elementary and complex plastic events, identified on the stress-strain curves, have been investigated. Although the pressure dependence of the activation barriers would be of interest, the calculation of transition paths also require heavier computational power. We therefore report energy barrier calculations at constant volume, corresponding to a pressure $-1 < P < 0$ GPa.

In Fig. 5, details of a stress-strain curve centered on two plastic events are shown. As expected for quasistatic deformations [42], linear elastic segments are interrupted by abrupt stress drops, which correspond to irreversible plastic events. Two critical values of the applied strain γ_c, at which the system reaches an instability, are highlighted in Fig. 5. In order to characterize the activation of these events, we calculated their energy barrier using the NEB method, as a function of $\gamma_c - \gamma$. The procedure was as follows. First, we selected two configurations before and after the instability. Starting from these configurations, we reversed the applied strain quasistatically as described in Sec. II, with a negative strain increment $\delta\gamma = -2\times10^{-5}$. We thus obtained pairs of equilibrium configurations at the same applied strain, one configuration before and the other after the plastic event. They correspond to pairs of green and red circles on the stress-strain curves of Fig. 5. NEB calculations were used to identify the minimum energy path (MEP) between these configurations from which the height of the energy barrier,

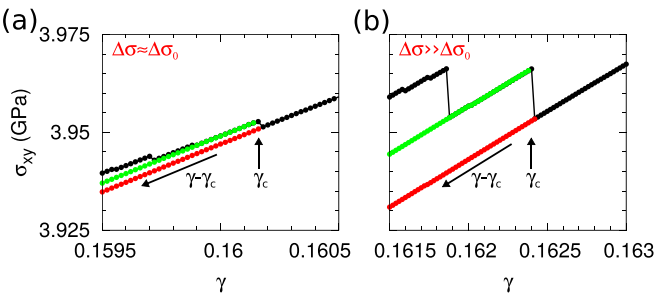

FIG. 5. Plastic stress drops due to (a) an isolated ST and (b) a cascade of STs are identified on the stress-strain curve at different critical shear strains γ_c. Pairs of equilibrium configurations, one before and the other after the plastic event, are shown as green and red circles, respectively, for different $\gamma - \gamma_c$ values.

which controls the plastic event, was calculated as well as the evolution of the plastic rearrangement along the MEP. The NEB method is a well-established technique to find the MEP and saddle point between given configurations [32,35]. Briefly, an initial path is constructed using a chain of intermediate configurations (called images), typically constructed by linear interpolation between the initial and final states. The energy along the chain is then minimized, keeping the distance between neighboring images constant by adding springs between images in configuration space. After minimization, the activation energy is obtained as the energy difference between the initial configuration and the image of maximum energy. We show in the following the results for two different scenarios: the first selected event [Fig. 5(a)] corresponds to the activation of an isolated ST, while the second event arises from a cascade of STs [Fig. 5(b)].

A. Activation of an isolated shear transformation

Isolated STs can be identified along the stress-strain curve by the amplitude of their stress variation. Indeed, we can estimate the amplitude of the stress drop induced by a single ST from its characteristic effective volume, Ω_0. Since the events analyzed here belong to the second regime, we can take $\Omega_0 = 25$ Å^3, and from Eshelby's model we have

$$|\Delta\sigma_0| = 2G\frac{\Omega_0}{V_{\text{cell}}}. \tag{3}$$

With $G = 25$ GPa, the shear modulus calculated in plastic transition regime (regime II) [12] and $V_{\text{cell}} = 660\,\text{nm}^3$, the simulation cell volume, we obtain $|\Delta\sigma_0| \sim 1.9$ MPa. In Fig. 5(a), the shear stress variation $\Delta\sigma_{xy}$ related to the discontinuity at $\gamma_c = 0.16$ is approximately -2 MPa, which makes such plastic event a good candidate to investigate the activation of an isolated shear transformation.

Results of the NEB calculations between the local minima before and after the plastic event at $\gamma_c = 0.16$ are shown in Figs. 6 and 7. The total number of images adopted in the NEB calculation is 100, and the strength of the NEB spring constant, 1 eV/Å^2. Relaxation of the NEB image configurations was stopped when the amplitude of the maximum force was lower

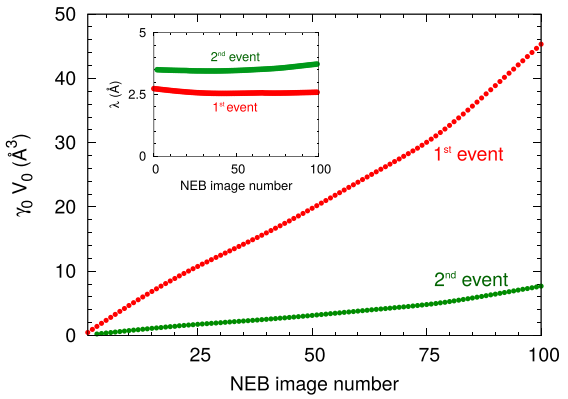

FIG. 6. Effective Eshelby volume $\gamma_0 V_0$ for the two most active STs identified along the NEB path calculated at $\gamma_c = 0.16$. Inset: characteristic size λ of the two STs.

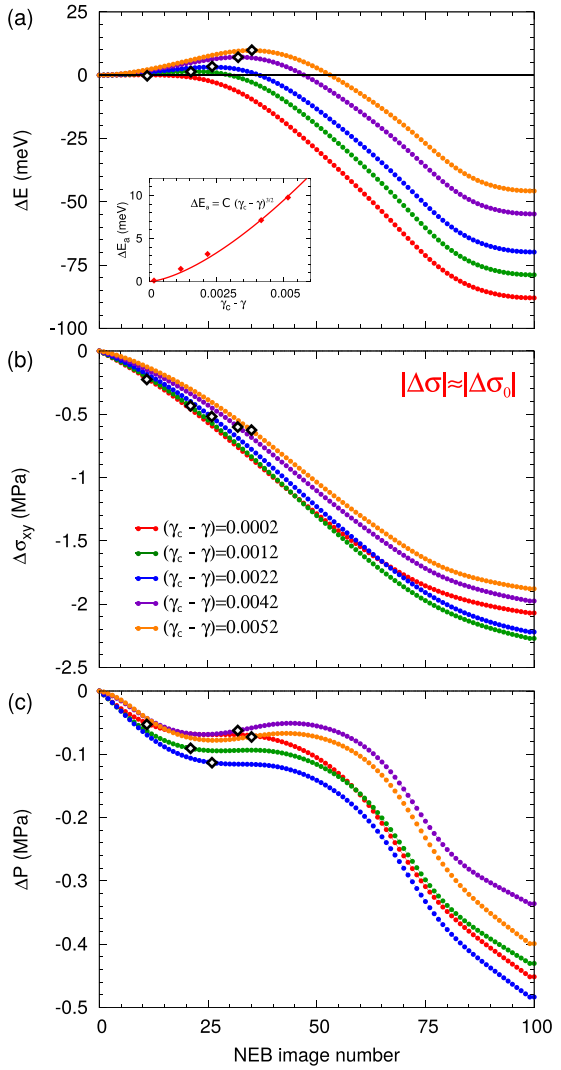

FIG. 7. Variation of the internal energy ΔE (a), shear stress $\Delta\sigma_{xy}$ (b), and pressure ΔP (c) along the NEB paths of the isolated ST, that occurred at $\gamma_c = 0.16$ in Fig. 5(a). The different curves were obtained at increasing values of $\gamma_c - \gamma$. Inset: Barrier height ΔE_a as a function of the distance from the instability. Empty diamonds are used to visualize the position of the activated state on each curve.

than 1×10^{-2} eV/Å. The initial chain of NEB images was obtained by linear interpolation of the atomic coordinates between the initial and final states. In order to verify that the plastic rearrangement identified at $\gamma_c = 0.16$ corresponds to a single ST, we performed the Eshelby analysis summarized in Sec. II along the NEB path.

The evolution of the characteristic size λ and effective volume $\gamma_0 V_0$ along the NEB path for the two most active events (i.e., the events characterized by the largest plastic activity) is reported in Fig. 6. We can see that the ST volume is constant along the path, justifying the usual assumption. Also, we can see from the effective volumes that one event clearly dominates the evolution of the plastic strain. We can thus examine this irreversible rearrangement as the activation of a single ST. Since the size of the ST core does not change along the path, the increase of the ST effective volume $\gamma_0 V_0$ in Fig. 6 is due

to a continuous increase of the plastic strain γ_0 along the NEB path, which reflects a continuous growth of the elastic field produced by the atomic displacements in the ST core.

The internal energy variation ΔE with respect to the initial configuration is shown in Fig. 7(a). The different curves were obtained at different values of $\gamma_c - \gamma$. The height of the energy barrier ΔE_a is plotted as function $\gamma_c - \gamma$ in the inset of Fig. 7. The energy barrier is zero at the instability ($\gamma = \gamma_c$) and increases as a power law with a 3/2 exponent expected for a saddle-node bifurcation [43]. The energy barrier is asymmetric, with the saddle configuration close to the initial configuration, rather than near the middle of the path as assumed for simple thermally-activated paths. The activated state moves toward the middle of the path as the distance from the instability increases, but its effective volume remains smaller than half the final effective volume, in contrast with the usual assumption made in mesoscale models [17].

The shear stress and pressure variations along the NEB path are reported in Figs. 7(b) and 7(c). The shear stress σ_{xy} decreases almost linearly along the paths, which is consistent with the evolution of the shear strain amplitude γ_0 reported in Fig. 6. The pressure difference ΔP also decreases along the path. There is a transient dilatation along the path, which is marked by a local relative increase of the pressure near the middle of the path. However, this transient dilatation occurs after the transition state, in contrast with simple hard-sphere models [6], which assume that the activated state corresponds to when atoms cross one another and thus corresponds to a maximum local dilatation in the glass. We repeated the same calculations with several other low-stress drop events corresponding to isolated STs and giving rise to either positive or negative total pressure variations. Along every calculated NEB paths, a transient volume expansion was found, but systematically after the activated state. We can therefore conclude that, at least for the a-Si glass studied here, a transient dilatation exists but is not directly connected to the activated state and therefore does not affect the pressure sensitivity of the activation energy. We also investigated the sensitivity of the activation barrier on the applied pressure but the latter is significantly weaker than the dependence on the shear stress. This prevented us to quantify the influence of P on Eq. (2) starting from the plastics events identified on the shear stress-strain curve.

B. Activation of a cascade of shear transformations

The activation of a first ST often triggers the activation of several others, potentially leading to an avalanche. To analyze this process, we selected an event at $\gamma_c = 0.1624$ in Fig. 5(b), with a stress drop amplitude ($|\Delta\sigma_{xy}| = 13.5$ MPa) much larger than the absolute value of the stress variation ($|\Delta\sigma_0| \sim 1.9$ MPa) characteristic of individual STs. The corresponding NEB calculations are shown in Figs. 8 and 9. We have checked by repeating the same calculations with other events that the present rearrangement is representative of large plastic events involving several STs.

Figure 8 shows the evolution of the effective volume of the four most active STs along the path computed at $\gamma = \gamma_c$. As can be seen, the STs do not appear simultaneously, but develop in stages. In particular, the stepwise growth of the

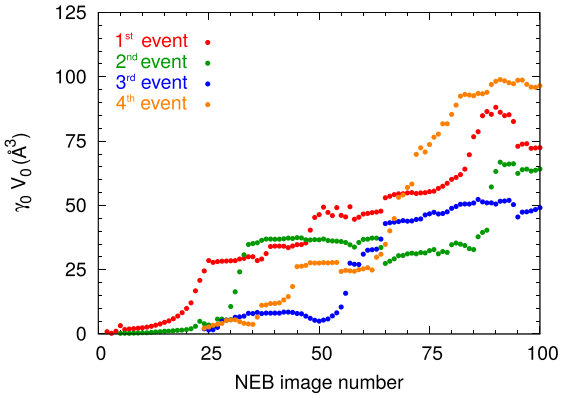

FIG. 8. Effective Eshelby volume $\gamma_0 V_0$ for the four most active STs identified along the NEB path characteristic of a plastic rearrangement involving several STs.

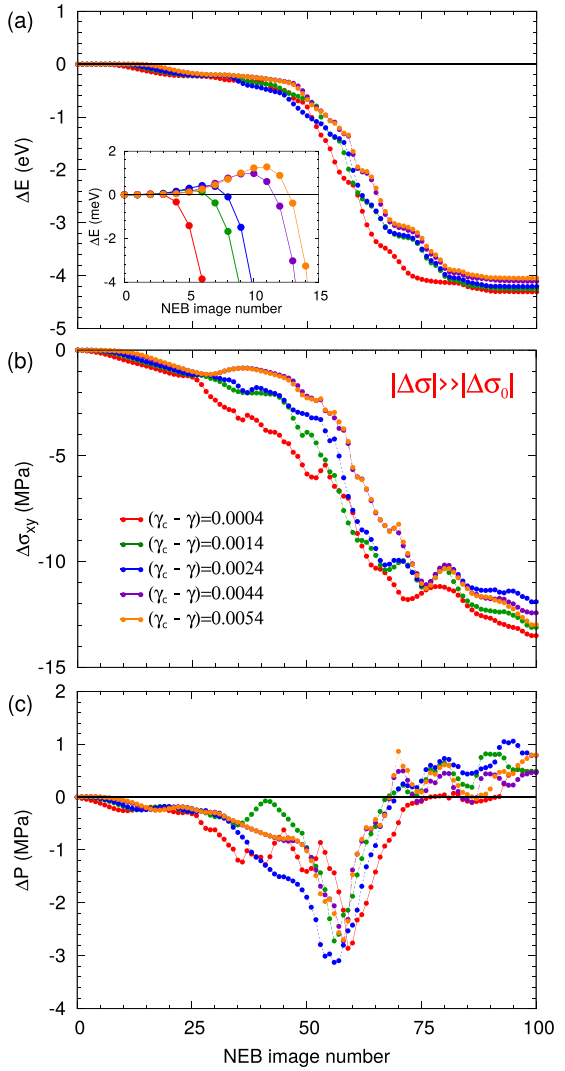

FIG. 9. Variation of the internal energy ΔE (a), shear stress $\Delta\sigma_{xy}$ (b), and pressure ΔP (c) along the NEB paths of the cascade of STs that occurred at $\gamma_c = 0.1624$ in Fig. 5(b). The different curves were obtained for increasing values of $\gamma_c - \gamma$. Inset: Magnification at the beginning of the energy path in (a), showing the growth of the energy barrier.

ST effective volumes suggests that the activation of one event is triggered by the expansion of a preceding event. The cooperative evolution of the plastic events is characterized by a rather complex activation path. In Fig. 9(a), we observe several bumps that can be assigned to the activation of successive STs. The inset of Fig. 9(a) shows that the energy barrier is located at the very beginning of the path, within the 15 first images, when there is a single active ST, as seen in Fig. 8. The energy barrier, therefore, corresponds to this very first ST, which then triggers the other events.

The footprints of consecutive activation of several STs is also visible on the shear stress and pressure curves [Figs. 9(b) and 9(c)]. The initial smooth decrease of the shear stress and smooth variation of the pressure correspond to the activation of the first event. After image ∼25, when new STs are activated, the shear stress and pressure curves start to vary rapidly, due to the concurrent activation of new STs and expansion of existing ones. The pressure curve is particularly intricate, with rapid positive and negative variations that result in a final positive pressure variation, i.e. a local volume expansion, but after a much larger transient contraction. Moreover, while the shear stress systematically decreases during plastic events, the final pressure variation can be either positive or negative. Interestingly, at the beginning of the path, when there is a single active ST (image number <25), the pressure first decreases and then slightly increases. This local dilatation occurs again after the activated state, consistent with the pressure evolution seen for an isolated ST in previous subsection. This corroborates the conclusion that, contrary to simple hard sphere models, the transitory dilatation occurs after the ST activated state and therefore does not affect its activation energy.

C. Activation volume

The activation paths of about 20 events, among which we identified both isolated and extended plastic rearrangements, have been studied by the NEB method. For such selected events, we obtained the energy profiles for different values of $(\gamma_c - \gamma)$ as in the two examples shown in Figs. 7(a) and 9(a). A first important parameter that we extracted is the activation barrier ΔE_a, i.e., the maximum energy difference between the NEB image and the initial configuration. Without exception, the energy barriers increased with the distance from the instability. At $\gamma_c - \gamma = 0.005$, ΔE_a values vary from 1 to about 10 meV. Barrier heights close to the instability remain small and represent approximately one tenth of the energy difference between the initial and final states in the case of isolated STs. The barrier associated with events involving several STs is of the same order of magnitude, if not slightly lower. This suggests that plastic events involving the cooperative action of several STs remain triggered by a single ST. Also, this points out that broad atomic rearrangements involving cascades of STs do not require to overcome higher barriers than isolated events.

A second quantity of interest extracted from the NEB calculations is the activation volume of the STs. Following a thermodynamic approach, the activation volume is given by the derivative of the energy barrier ΔE_a with respect to the applied shear stress σ_{xy}. Furthermore, by taking advantage of the linear relationship between stress and strain in the elastic segments leading to the plastic instabilities, we can express ΔV_a as a function of the distance from the instability:

$$\Delta V_a = -\frac{\partial \Delta E_a}{\partial \sigma_{xy}} = -\frac{\partial \Delta E_a}{\partial \varepsilon_{xy}} \frac{\partial \varepsilon_{xy}}{\partial \sigma_{xy}} = \frac{\partial \Delta E_a}{\partial (\gamma_c - \gamma)} \frac{1}{G}. \quad (4)$$

As mentioned above, the identified energy barriers follow the scaling relation $\Delta E_a = C(\gamma_c - \gamma)^{3/2}$ expected close to a saddle-node bifurcation. By inserting this analytic expression in Eq. (4), we find the following scaling law for ΔV_a:

$$\Delta V_a = \frac{3}{2} \frac{C}{G} (\gamma_c - \gamma)^{1/2}. \quad (5)$$

Inspired by Argon's model [6] and Eq. (2), the activation volume can also be expressed as the ST effective Eshelby volume $\gamma_0^* V_0$ computed at the activated state along the NEB path, as shown in Figs. 6 and 8:

$$\Delta V_a = (\gamma_0 V_0)^* \sim V_0 \gamma_0^*, \quad (6)$$

since the ST volume does not vary significantly along the paths.

In Fig. 10, we plotted ΔV_a as a function of $(\gamma_c - \gamma)$ as obtained by using both definitions of Eqs. (4) and (6). The solid curves are obtained by fitting parameter C in Eq. (5) to the data calculated by following the thermodynamic approach (red circles). The results obtained following both approaches are in remarkable agreement. Also, the scaling law in Eq. (5) reproduces correctly the evolution of ΔV_a with $(\gamma_c - \gamma)$. A noteworthy result is that the effective Eshelby volume at the saddle point corresponds effectively to the activation volume obtained from the thermodynamic approach. Furthermore, we find that the activation volumes correspond to a fraction of the effective Eshelby volume at the final state, $\gamma_0 V_0$. For example, ΔV_a is 17 and 2 Å^3 for the two selected events at $\gamma_c - \gamma = 0.005$ (see Fig. 10), while $\gamma_0 V_0$ in the final states is 45 and 75Å^3, respectively.

The activation volume for large plastic events ($|\Delta\sigma| \gg |\Delta\sigma_0|$) coincides with the effective Eshelby volume of the first

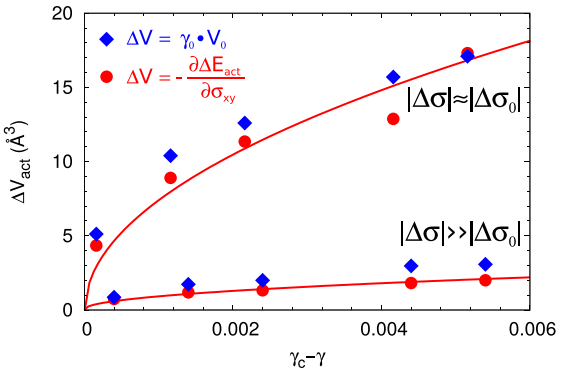

FIG. 10. ST activation volume calculated in two different ways: as the negative derivative of the energy barrier ΔE_a with respect to the shear stress σ_{xy} (red circles) and as the Eshelby effective volume $\gamma_0^* V_0$ of the first plastic event identified along the NEB path computed at the saddle point (blue diamonds). Activation volumes are calculated for an isolated ST (top curve, $|\Delta\sigma| \sim |\Delta\sigma_0|$) and for a cascade of STs (bottom curve, $|\Delta\sigma| \gg |\Delta\sigma_0|$).

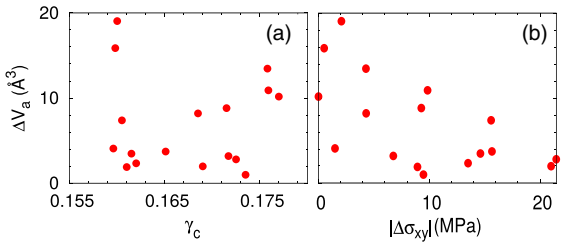

FIG. 11. Activation volume as a function of γ_c (a) and of shear stress drop amplitude produced by the plastic event $|\Delta\sigma_{xy}|$ (b). ΔV_a is calculated as the negative derivative of the energy barrier ΔE_a with respect to the shear stress σ_{xy} at $(\gamma_c - \gamma) = 0.005$ for several plastic events involving either isolated or cascades of STs.

activated ST, demonstrating again that the first ST triggers the subsequent avalanche. Furthermore, the activation volume for large plastic events is significantly smaller than for isolated STs, even though the final effective volume is larger. To check this correlation more quantitatively, we reported in Fig. 11 the distribution of activation volumes calculated at $(\gamma_c - \gamma) = 0.005$ as a function of γ_c in Fig. 11(a) and of $|\Delta\sigma_{xy}|$ in Fig. 11(b), i.e., the amplitude of the stress drop induced by the plastic event. Values of ΔV_a at $(\gamma_c - \gamma) = 0.005$ can be considered as a sensible measure of the activation volumes since the activation volume scales as $(\gamma_c - \gamma)^{1/2}$ [see Eq. (5)] and therefore increases slowly away from the instability. Values between 2 and 20 Å^3 are found. Since both isolated STs and complex plastic events of different sizes were considered, this gives estimates of the upper and lower bounds of ΔV_a.

We see in Fig. 11(a) that there is no correlation between the activation volume and the deformation value. On the other hand, Fig. 11(b) shows a decreasing trend of the activation volume with increasing stress drops $|\Delta\sigma_{xy}|$, which is a signature of the extent of the collective plastic reorganization. Therefore, isolated STs which produce small plastic deformations are characterized by a higher activation volume than STs, which induce cascades of STs and large plastic deformations. This correlation may be a manifestation of the deformation history of the a-Si sample. The smaller activation volume associated with extended plastic rearrangements indicate the development of regions where STs are favored, i.e., easier to shear.

V. CONCLUSIONS

In summary, we investigated the impact of damage, pressure and glass-relaxation on the characteristics of the shear transformation zones in an a-Si model. We also presented the detailed activation mechanism coupled with the STs analysis on some representative single and collective plastic events.

We showed that the asymmetric behavior of a-Si under tension or compression condition is linked to the elementary operation mechanism of STs. While the higher strength of metallic glasses under compression is attributed to a temporary volume expansion involved in ST activation, in the present a-Si samples, STs inducing volume contraction are favored with respect to those that promote volume expansion. The transitory dilatation predicted from ST theory is found systematically after the activated state, suggesting that it does not affect the plastic properties in this material. Even though this result is peculiar to the SW potential, it demonstrates that bond character and directionality have an impact on the shear transformation process. This elementary mechanism in turn, may affect the response under pressure or normal-stress components of diverse glasses, e.g., oxide or silica glasses.

Decaying exponential distributions of the effective ST volumes, $V_0\gamma_0$, are found, justifying the common assumption made in mesoscale models of constant γ_0 and V_0 values. However, the characteristic size of these distributions increases with the level damage, which can be induced by plastic activity, rapid quenching, and especially by the localization of the deformation in shear bands. On the contrary, such distributions are not strongly affected by pressure or normal stress components. Moreover, we extracted the activation energy and volume, which integrated in mesoscale models may give access to thermal effects and strain-rate sensitivity. Interestingly, the activation volume associated with isolated STs and extended plastic reorganizations produced by avalanches corresponds to the effective Eshelby volume calculated at the saddle point of the initial, and possibly only, ST involved in the plastic event. The measured activation volume corresponds to a fraction of the effective Eshelby volume in the final sheared state. Additionally, smaller activation volumes are found for avalanches, suggesting that damage has also a strong impact on the activation properties of STs, although the question of how to quantify structural damage in glassy systems remains an open question.

[1] W. L. Johnson, J. Miner. Metals Mater. Soc. **54**, 40 (2002).
[2] C. A. Schuh, T. C. Hufnagel, and U. Ramamurty, Acta Mater. **55**, 4067 (2007).
[3] A. L. Greer, Mater. Today **12**, 14 (2009).
[4] P. Steif, F. Spaepen, and J. Hutchinson, Acta Metall. **30**, 447 (1982).
[5] A. Argon and H. Kuo, Mater. Sci. Eng. **39**, 101 (1979).
[6] A. Argon, Acta Metall. **27**, 47 (1979).
[7] D. Srolovitz, V. Vitek, and T. Egami, Acta Metall. **31**, 335 (1983).
[8] M. L. Falk, Phys. Rev. B **60**, 7062 (1999).
[9] E. R. Homer and C. A. Schuh, Acta Mater. **57**, 2823 (2009).
[10] M. L. Falk and J. S. Langer, Phys. Rev. E **57**, 7192 (1998).
[11] A. Tanguy, F. Leonforte, and J. L. Barrat, Eur. Phys. J. E **20**, 355 (2006).
[12] T. Albaret, A. Tanguy, F. Boioli, and D. Rodney, Phys. Rev. E **93**, 053002 (2016).
[13] C. Fusco, T. Albaret, and A. Tanguy, Phys. Rev. E **82**, 066116 (2010).
[14] P. Schall, D. A. Weitz, and F. Spaepen, Science **318**, 1895 (2007).
[15] V. V. Bulatov and A. S. Argon, Modell. Simul. Mater. Sci. Eng. **2**, 167 (1994).
[16] G. Picard, A. Ajdari, F. Lequeux, and L. Bocquet, Phys. Rev. E **71**, 010501 (2005).
[17] E. R. Homer, D. Rodney, and C. A. Schuh, Phys. Rev. B **81**, 064204 (2010).

[18] D. Vandembroucq and S. Roux, Phys. Rev. B **84**, 134210 (2011).
[19] K. Martens, L. Bocquet, and J.-L. Barrat, Phys. Rev. Lett. **106**, 156001 (2011).
[20] S. Sandfeld, Z. Budrikis, S. Zapperi, and D. F. Castellanos, J. Stat. Mech. (2015) P02011.
[21] J. D. Eshelby, Proc. Roy. Soc. London A **241**, 376 (1957).
[22] M. Talamali, V. Petäjä, D. Vandembroucq, and S. Roux, Comptes Rendus Mecanique **340**, 275 (2012).
[23] A. Nicolas, K. Martens, and J.-L. Barrat, Europhys. Lett. **107**, 44003 (2014).
[24] L. Li, E. R. Homer, and C. A. Schuh, Acta Mater. **61**, 3347 (2013).
[25] D. Rodney, A. Tanguy, and D. Vandembroucq, Modell. Simul. Mater. Sci. Eng. **19**, 083001 (2011).
[26] D. Rodney and C. A. Schuh, Phys. Rev. Lett. **102**, 235503 (2009).
[27] P. Koziatek, J.-L. Barrat, P. Derlet, and D. Rodney, Phys. Rev. B **87**, 224105 (2013).
[28] S. Patinet, D. Vandembroucq, and M. L. Falk, Phys. Rev. Lett. **117**, 045501 (2016).
[29] C. A. Schuh and A. C. Lund, Nat. Mater. **2**, 449 (2003).
[30] A. Lund and C. Schuh, Intermetallics **12**, 1159 (2004).
[31] A. Argon and L. Shi, Acta Metall. **31**, 499 (1983).
[32] H. Jónsson, G. Mills, and K. W. Jacobsen, in *Classical and Quantum Dynamics in Condensed Phase Simulations*, edited by B. J. Berne, G. Ciccotti, and D. F. Coker (World Scientific, Singapore, 1998), pp. 385–404.
[33] F. H. Stillinger and T. A. Weber, Phys. Rev. B **31**, 5262 (1985).
[34] M. P. Allen and D. J. Tildesley, *Computer Simulation of Liquids* (Oxford University Press, Oxford, UK, 1989).
[35] G. Henkelman and H. Jónsson, J. Chem. Phys. **113**, 9978 (2000).
[36] G. Henkelman, B. P. Uberuaga, and H. Jónsson, J. Chem. Phys. **113**, 9901 (2000).
[37] W. D. Luedtke and U. Landman, Phys. Rev. B **40**, 1164 (1989).
[38] M. J. Demkowicz and A. S. Argon, Phys. Rev. B **72**, 245206 (2005).
[39] D. Deng and B. Lu, Scr. Metall. **17**, 515 (1983).
[40] K. Hajlaoui, T. Benameur, G. Vaughan, and A. Yavari, Scr. Mater. **51**, 843 (2004).
[41] M. Talati, T. Albaret, and A. Tanguy, Europhys. Lett. **86**, 66005 (2009).
[42] C. Maloney and A. Lemaitre, Phys. Rev. Lett. **93**, 195501 (2004).
[43] C. E. Maloney and D. J. Lacks, Phys. Rev. E **73**, 061106 (2006).